INTERNATIONAL JOURNAL OF HYDROGEN ENERGY 45 (2020) 26746–26757

Available online at www.sciencedirect.com

ScienceDirect

journal homepage: www.elsevier.com/locate/he

Nanostructured Ni:$BiVO_4$ photoanode in photoelectrochemical water splitting for hydrogen generation

Sakshi Saxena [a], *Anuradha Verma* [a], *Kumari Asha* [a], *Neeraj Kumar Biswas* [a], *Anamika Banerjee* [a], *Vibha Rani Satsangi* [b], *Rohit Shrivastav* [a], *Sahab Dass* [a,*]

[a] *Department of Chemistry, Dayalbagh Educational Institute, Dayalbagh, Agra, 282005, India*

[b] *Department of Physics and Computer Science, Dayalbagh Educational Institute, Dayalbagh, Agra, 282005, India*

HIGHLIGHTS

- Ni doping on $BiVO_4$ with respect to phosphate buffer electrolyte studied first time.
- Nanoporous morphology with particles arranged in linear and branched manner.
- 136 times increment in J_{ph} observed as compared to pristine samples.
- Presence of hole scavenger enhanced hydrogen production rate.

GRAPHICAL ABSTRACT

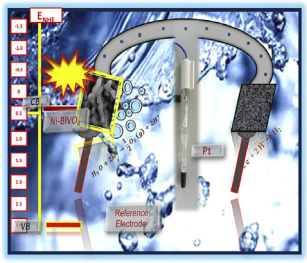

ARTICLE INFO

Article history:
Received 3 May 2020
Received in revised form
1 July 2020
Accepted 8 July 2020
Available online 30 July 2020

Keywords:
Photoelectrochemical (PEC) splitting of water
Electrodeposited Ni doped $BiVO_4$
ABPE

ABSTRACT

Photoelectrochemical water splitting using bismuth vanadate ($BiVO_4$) is drawing attention but on account of presence of high charge recombination and poor water oxidation kinetics its performance is restricted. Present study attempts to understand the role of dopant Ni on $BiVO_4$ in a) reducing the charge recombination and b) to improve water oxidation kinetics. Ni doped $BiVO_4$ thin films are prepared via electrodeposition method and photoelectrochemical properties are investigated in 0.1 M phosphate buffer solution with and without sodium sulfite hole scavenger. Photocurrent density of 1.36 mA/cm^2 at 1.23 V vs. RHE has been obtained using 1.5% Ni doped $BiVO_4$. This sample also offered lower flat band potential, high open circuit potential and applied bias photon-to-current conversion efficiency. Addition of hole scavenger significantly increases the photoelectrochemical performance. Ni as a dopant therefore can play an important role in not only suppressing the

* *Corresponding author.*
E-mail address: drsahabdas@gmail.com (S. Dass).
https://doi.org/10.1016/j.ijhydene.2020.07.080

Hole scavenger
Phosphate buffer

electron-hole pair recombination but also in offering significantly enhanced photoelectrochemical response.

Introduction

Majority of the worlds energy demand is fulfilled from fossil fuels but the depletion of these fossil fuels is quickly overfilling our ambiance with excessive volumes of CO_2 and other green house gases which are the culprit for global climate change [1–4]. About 90% of the world's energy demand is executed from the carbon-based fossil fuels and it is desirable to switch to a long-lasting and renewable energy source which is unadulterated and does not produce any greenhouse gases [5–7]. In this context and in view of establishing a renewable energy source, photoelectrochemically generated hydrogen using sunlight is considered as one of the ideal, most efficient and one-step process for splitting water into H_2 and O_2 [8–14].

PEC water splitting is also recognized as artificial photosynthesis, in which H_2 and O_2 are produced by a light-absorbing semiconductor electrode which offer a truly sustainable way of converting solar energy into chemical energy ($\Delta G^o = 237.1$ kJ/mol) [9,12,15–20].

$$H_2O_{(liquid)} + 2h\vartheta \rightarrow H_{2(gas)} + \frac{1}{2}O_{2(gas)} \quad (1)$$

The heart of PEC cell is the semiconductors which plays important role in executing the process of photoelectrochemical water splitting and the semiconductor should satisfy the following criteria-low bandgap with absorption in the visible region, efficient charge separation, straddling water redox potential, stability in aqueous and alkaline medium, etc [21–25]. Two types of semiconductor materials are known: low bandgap semiconductor (Fe_2O_3, CuO, $BiVO_4$, etc.) and high bandgap semiconductor (ZnO, $SrTiO_3$, TiO_2, etc.). Among hundreds of semiconductors known, none of the semiconductor fulfill all the above said requirements because in case of low band gap materials instability occurs due to the electron-hole pair recombination while absorption of a small portion of visible light in case of high band gap material is a big issue, therefore scientists across the globe are working together to find a suitable semiconductor which can accomplish all the above-said necessities.

Polycrystalline $BiVO_4$ is attracting significant consideration as an oxygen evolution photoanode in photoelectrochemical (PEC) water splitting owing to its important characteristics such as low bandgap (2.4 eV), absorption in the visible region, nontoxic, and stabile in neutral medium etc [26–31]. The improved photoactivity among the reported phase of $BiVO_4$ is shown by scheelite monoclinic over the scheelite zircon and tetragonal zircon. This is due to the Bi^{3+} lone pair distortion. The only difference between scheelite monoclinic (2.4 eV), scheelite tetragonal (2.4 eV) and zircon tetragonal (2.9 eV) is the bonding of Bi with VO_4 units as in the former Bi is bounded to eight VO_4 tetrahedral units while in the later it is bound to six VO_4 tetrahedral units [19,32–36]. Besides this the main barrier that reduce its performance are poor electron transport as well as electron-hole pair recombination. To conquer these limitations, a number of modification strategies such as doping [37–42], formation of heterojunction [26,43–48], application of MWCNT [35,49,50], use of co-catalyst [18,19,27,42,51–54], formation of homojunction [55] have been tried over a phase of time. Among various modifications, doping by Si, Ge, W, V, Mo, Pt, Cu, Zn, etc. is preferred as it enhances the carrier concentrations and conductivity which further increases the PEC performance [43,44]. Literature review of the work done by different groups of researchers is summarized below. Wan et al. investigated the role of W doped $BiVO_4$ and graphene modified W doped $BiVO_4$ for photoelectrochemical analysis and found that photocurrent increased 3.96 times in comparison to pristine sample [49]. Hernandez et al. observed 3 mA/cm^2 photocurrent density at 1.23 V vs. RHE (neutral medium) by Co-Pi modified $BiVO_4$ [19]. Kim and Lee discussed three modification techniques (heterojunction, addition of charge transfer mediator and deposition of Co-catalyst) in $BiVO_4$ [24]. Introducing the concept of gradient doping, Abdi et al. studied the gradient doping effect on Co-Pi catalyzed, W doped $BiVO_4$ and observed that 10 step gradient doped Co-Pi catalyzed, W doped $BiVO_4$ offers 4.9% STH efficiency [42].

Present communication deals with the effect of Ni doping on $BiVO_4$ prepared by electrodeposition method to better understand the role of Ni in PEC water splitting and experimentation has been carried out in phosphate buffer electrolyte. Ni and V belong to the same period in the periodic table and have similar chemical properties. Therefore doping with Ni is expected to offer some change on the crystal structure. Ni doped $BiVO_4$ has recently been reported by Regmi et al. in waste water treatment and apply DFT calculations on it. After the theoretical calculations, they observed that substitution of Ni with V gives more stable configuration and formation energy of Ni doping with V site with an adjacent oxygen vacancy is less than that of Bi. These results show that Ni doping at V site is more favorable. Further, the ionic radius of V^{5+} (0.059 nm) is comparable with Ni^{2+} (0.069 nm), it can easily replace V^{5+} from the crystal lattice without disturbing the lattice structure and is expected to form Bi–Ni–O bond [39,40]. Also, Ni^{2+} has 8 electrons in 3 d subshell against zero electron in V^{5+}, hence these extra electrons would increase the conductivity which may eventually increase the PEC response.

Experimental details

Materials and methods

Electrodeposition method reported by Kim et al. was used for the preparation of $BiVO_4$ on FTO substrate (1.2 cm × 1.5 cm) by Ref. [53] in which first step is the preparation of BiOI using cyclic voltammetry at a bias voltage of −0.145 V vs. SCE. Vanadium precursor was then deposited over the BiOI films which were then sintered in a tubular furnace at a temperature of 450 °C for 2 h. In case of preparation of Ni–$BiVO_4$, Nickel Nitrate hexahydrate was (as a Ni precursor with varying atomic percentage from 0.5% to 3.0%) dissolved in vanadium precursor and deposited over the BiOI film [39]. The detailed acronyms of the prepared thin films are given in Table 1.

Characterizations

Structural, optical and compositional analysis

Glancing angle X-ray diffractometer (Bruker AXS D8 Advance) using Cu Kα radiation source (k = 1.5418 Å) at a scan speed of 2 mV/s varying 2Θ value from 10° to 60° was used for crystal phase analysis. The optical behavior of the films was investigated by the absorbance data collected in the wavelength range of 400–800 nm with the help of UV–visible spectrophotometer (UV-1800, Shimadzu, Japan, Double Beam UV visible spectrophotometer). By utilizing the absorbance-wavelength data the bandgap of the deposited thin films was calculated using tauc plots. The oxidation states of Ni, Bi, V and O were investigated with X-ray Photoelectron spectroscopy (PHI Versa Probe II with AES). The binding energies were calculated with respect to C lines. To analyze the surface morphology and elemental composition, Field Emission Scanning electron microscopy (FE-SEM) using TESCAN MIRA II LMH system in connection with Energy Dispersive X-Ray Spectroscopy (EDX) was used. Phase analysis of the prepared thin films was evaluated using Raman Microscopy (RENISHAW).

Electrochemical and photoelectrochemical measurements

In order to measure the electrochemical and photoelectrochemical properties, the prepared thin films were converted into the electrode with the help of Cu wire, silver paste and non conducting epoxy resin (Hysole, Singapore). A typical three-electrode cell consisting of a reference electrode (saturated calomel electrode), the counter electrode (Pt electrode) and a working electrode (Ni–$BiVO_4$) was employed for this analysis. 0.1 M Potassium Phosphate buffer (KPi) solution was used as electrolyte with and without the presence of hole scavenger [52,53,57–59] which while acting as electron donor not only enhances the hydrogen production rate but also increase the quantum efficiency by scavenging the photogenerated holes of valence band. The current vs. potential spectrum under dark and illumination was recorded using electrochemical workstation (Zahner Zennium, Germany) by providing a bias of −1 to 1 V vs. SCE (−0.346 to 1.65 V vs. RHE) with a scan speed of 20 mV s^{-1}. A 150 W Xenon Arc Lamp with illumination intensity of 100 mW cm^{-2} (Oriel, USA) was used as light source and the applied potential for the analysis was converted into RHE using the following equation [44]:

$$E_{RHE} = E_{SCE} + 0.242 + 0.059*pH \quad (2)$$

Applied bias photon to current conversion efficiency (ABPE) which is also known as diagnostic efficiency, redirects the net generation of current by providing external bias through the abstraction of electrons from the electrode. It is calculated using photocurrent density (PCD) and open circuit potential (V_{OC}) data in the following equation [10,16,44]:

$$ABPE(\%) = \{(J_{Ph}(mA\ cm^{-2}) \times [1.23 - V_{app}(V)] \times) / P(mA\ cm^{-2})\} \times 100 \quad (3)$$

where J_{ph} = Photocurrent density per unit area (Light current-dark current/area of the electrode), $V_{app} = V_{meas}$-V_{oc} (V_{meas} is the potential at which J_{ph} was recorded and V_{oc} is the open circuit potential), P = illumination intensity of the light source.

Charge transfer kinetics at semiconductor/electrolyte interface was investigated with the help of Mott-Schottky and EIS experiments (Nyquist plots) in the potential range of -1 V to 1 V (vs. SCE) with 1 kHz frequency and 5 mV amplitude. The flat band potential was calculated by plotting a graph between $1/C^2$ and the applied potential (V_{app}) using the equation [11,21]:

$$\frac{1}{C^2} = \frac{2}{q\varepsilon\varepsilon_0 N_D}\left(V_{app} - V_{FB} - \frac{KT}{q}\right) \quad (4)$$

where C is the space charge capacitance, q is the charge, ε is the dielectric constant of the electrode, ε_0 is the permittivity of the vacuum, N_D is the donor density, V_{app} is the applied potential, V_{FB} is the flat band potential, k is Boltzmann's constant and T is the temperature.

The stability test of the best performing sample was done using chronoamperometry analysis for 1 h. The charge separation and injection efficiency of the electrode was calculated by measuring the photocurrent in presence and absence of a hole scavenger (Na_2SO_3) [21,60].

Table 1 – Description of the electrodeposited thin films.

Sample Description	Acronym
Pristine $BiVO_4$	P1
0.5% Ni doped $BiVO_4$	N1
1.0% Ni doped $BiVO_4$	N2
1.5% Ni doped $BiVO_4$	N3
2.0% Ni doped $BiVO_4$	N4
2.5% Ni doped $BiVO_4$	N5
3.0% Ni doped $BiVO_4$	N6

Results and discussion

Phase analysis

Structural analysis of the prepared P1 and N3 thin film was evaluated with the help of XRD spectrum (Fig. 1). The highest intensity peak at 28.7° corresponding to (121) plane confirms

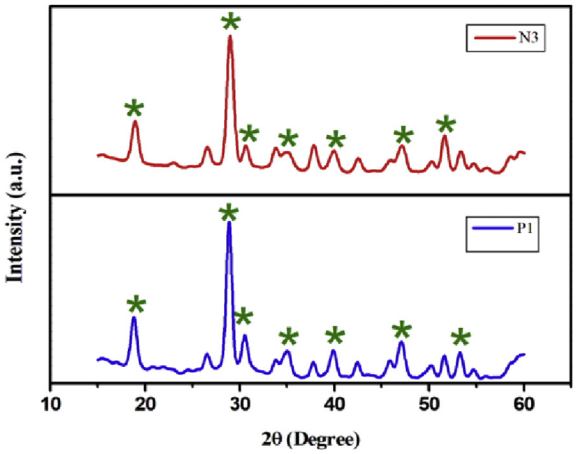

Fig. 1 – XRD pattern of pristine $BiVO_4$ (P1) and Ni–$BiVO_4$ (N3) thin films.

the scheelite monoclinic phase of $BiVO_4$ which is in good agreement with the values reported by Shrivastav et al. [55], Cheng et al. [26] and matches well with JCPDS card no. 140688. For the Ni doped $BiVO_4$ (N3), slight change in the highest peak position and intensity is visible due to the Ni doping. The enlarged view of maximum intensity peak for P1 and N3 is shown in Fig. S1 (Supplementary Information). In Fig. 1 peaks marked by asterisk (*) corresponds to $BiVO_4$ while all other peaks corresponds to FTO substrate.

Optical absorbance analysis

Photoelectrochemical performance of the samples also depend upon the optical properties of semiconductor [61]. UV–vis graph for P1 and N3 is shown in Fig. 2(a) which clearly shows that both the sample have absorbance in the visible region (520 nm) and corresponds to the band gap of 2.4 eV (Fig. 2 (b and c)) [26,31,36,61,62]. For all other samples the absorbance spectra and band gap calculated from Tauc plot are shown in Fig. S2 (Supplementary Information) and Table 2.

Raman Analysis

To confirm the monoclinic phase of $BiVO_4$, Raman analysis was performed in the range of 100–1000 cm^{-1} as shown in Fig. 3. Characteristic Raman peaks at 126, 210, 321, 365 and 830 cm^{-1} confirm the formation of monoclinic phase.

Table 2 – V_{OC}, Band gap and V_{FB} of the electrodeposited thin films.

Sample description	Open circuit potential (V_{OC}) vs. RHE	Band gap (eV)	Flat band potential (V_{FB} vs. RHE)
P1	0.75	2.4	0.42
N1	0.85	2.5	0.57
N2	0.90	2.5	0.55
N3	0.95	2.4	0.37
N4	0.93	2.4	0.45
N5	0.91	2.4	0.48
N6	0.92	2.5	0.46

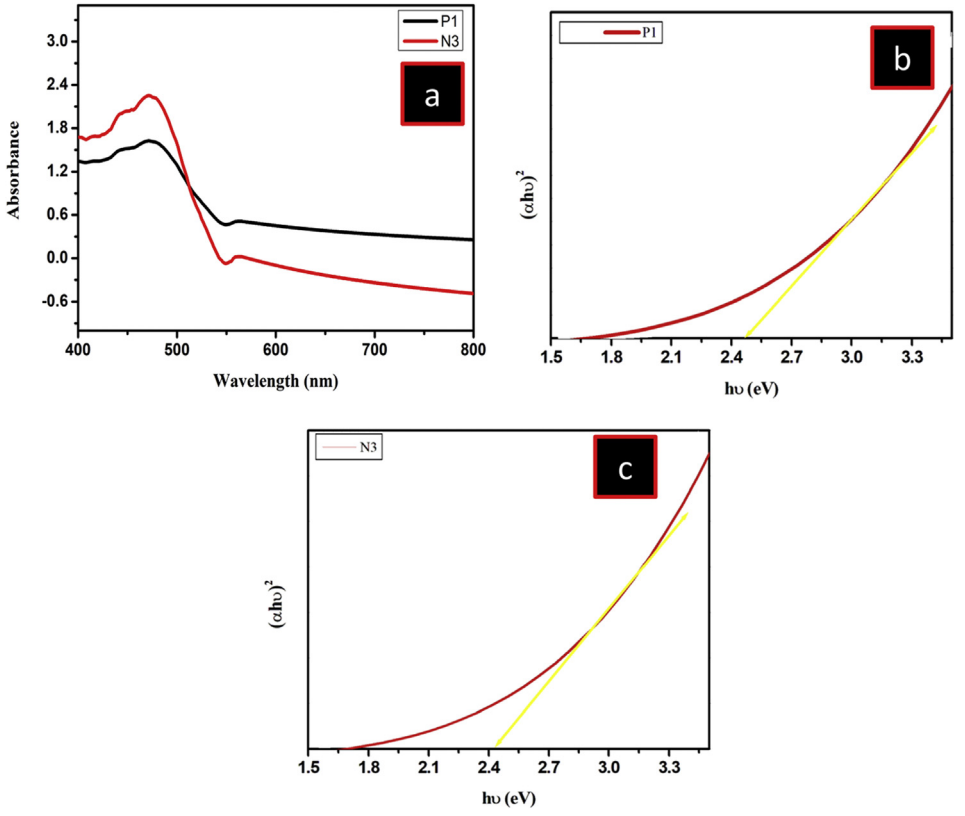

Fig. 2 – (a) UV–vis absorption spectra and (b–c) Tauc plots of pristine $BiVO_4$ (P1) and Ni–$BiVO_4$ (N3) thin films.

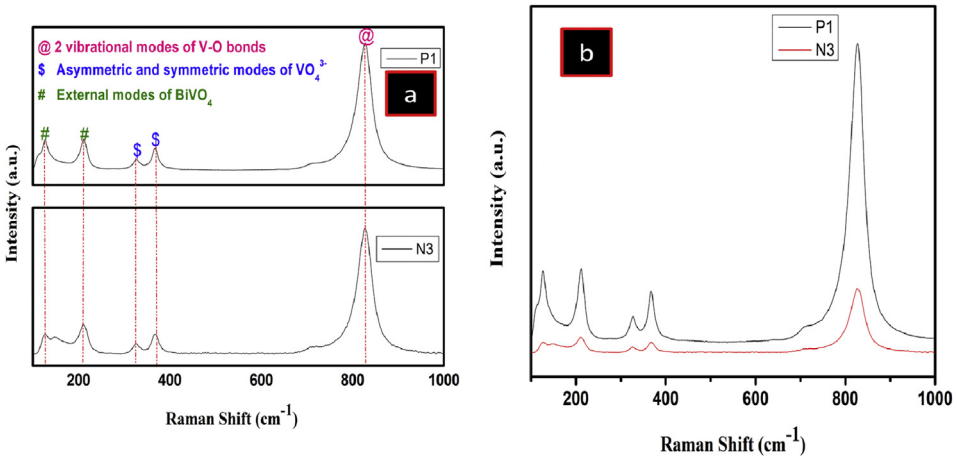

Fig. 3 – (a,b) Raman spectra of pristine $BiVO_4$ (P1) and Ni–$BiVO_4$ (N3) thin films.

Structural information was obtained from the Raman peaks at 126 and 210 cm^{-1}. Peaks at 321 and 365 cm^{-1} shows the asymmetric and symmetric modes of VO_4^{3-} tetrahedron and peak at 830 cm^{-1} correspond to the two other vibrational modes of V–O bonds [19,26,30]. In doped samples significant broadening and decrease in intensity was observed (Fig. 3 (b)).

Morphological and compositional analysis

Morphology of the prepared $BiVO_4$ and Ni doped $BiVO_4$ thin films were evaluated using field emission scanning electron microscopy (FE-SEM) and results are shown in Fig. 4(a). From the figure it is clear that nanoporous layered morphology of $BiVO_4$ was obtained over the FTO substrate while for Ni doped $BiVO_4$, nanoporous morphology was obtained in which granular particles are arranged in linear and branched manner (Fig. 4 (b) [56,69]. The corresponding SEM images in micrometer range are shown in Fig. S3 (Supplementary Information).

Compositional analysis of the prepared thin films were evaluated from EDX analysis. EDX spectrum shown in Fig. S6 (Supplementary Information) confirms the presence of B, V, O, Ni and Sn with the atomic percentage of 9.61%, 9.69%, 76.42%, 1.00% and 3.29% respectively and undoubtedly indicate that B to V ratio is 1:1 while Sn in the EDX spectrum is due to underlying FTO.

The chemical states of the pristine $BiVO_4$ and Ni–$BiVO_4$ were also evaluated with the help of XPS. As shown in the XPS spectra (Fig. 5) only Bi, V, O, Ni and C was observed. C in the spectrum is comes from as a base, all the binding energies were calculated using C as a base line. In the XPS spectrum, the binding energy at 158.9eV, 164.2 eV was attributed to Bi ($4f_{7/2}$, $4f_{5/2}$) and confirms that Bi is present as Bi^{3+}. The peaks at 516.5eV, 523.8 eV corresponds to V ($2p_{3/2}$, $2p_{1/2}$) with +5 oxidation states. Further, the peak at 516.1eV corresponds to V^{4+}cations, respectively. This is due to the ionic radii difference between Ni, Bi and V which confirm that some of the V^{5+} replaced by Ni^{2+} and form Bi–Ni–O bond. The binding energy at 856.4 eV and 874.1 eV correspond to $Ni2p_{3/2}$ and $Ni2_{p1/2}$. This value clearly shows that Ni is not present as NiO in the $BiVO_4$ [39,40].

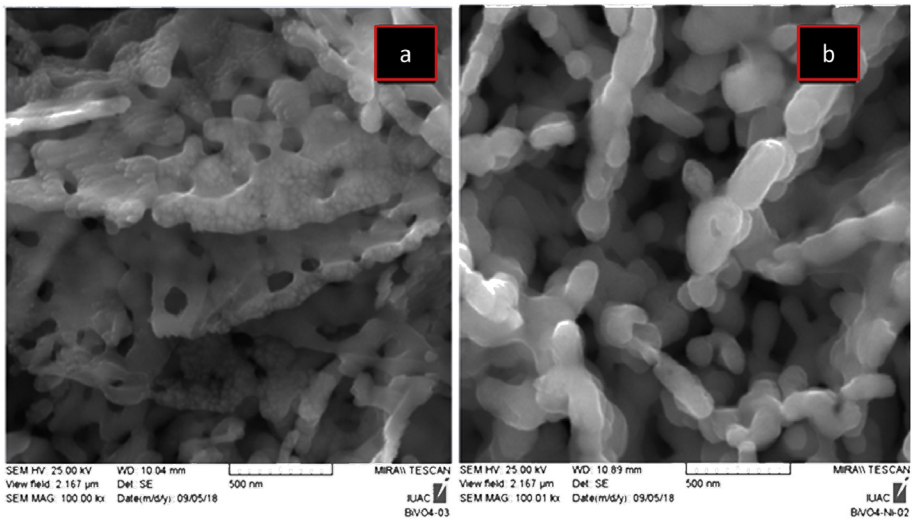

Fig. 4 – (a,b) FE-SEM images of pristine $BiVO_4$ (P1) and Ni–$BiVO_4$ (N3) thin films.

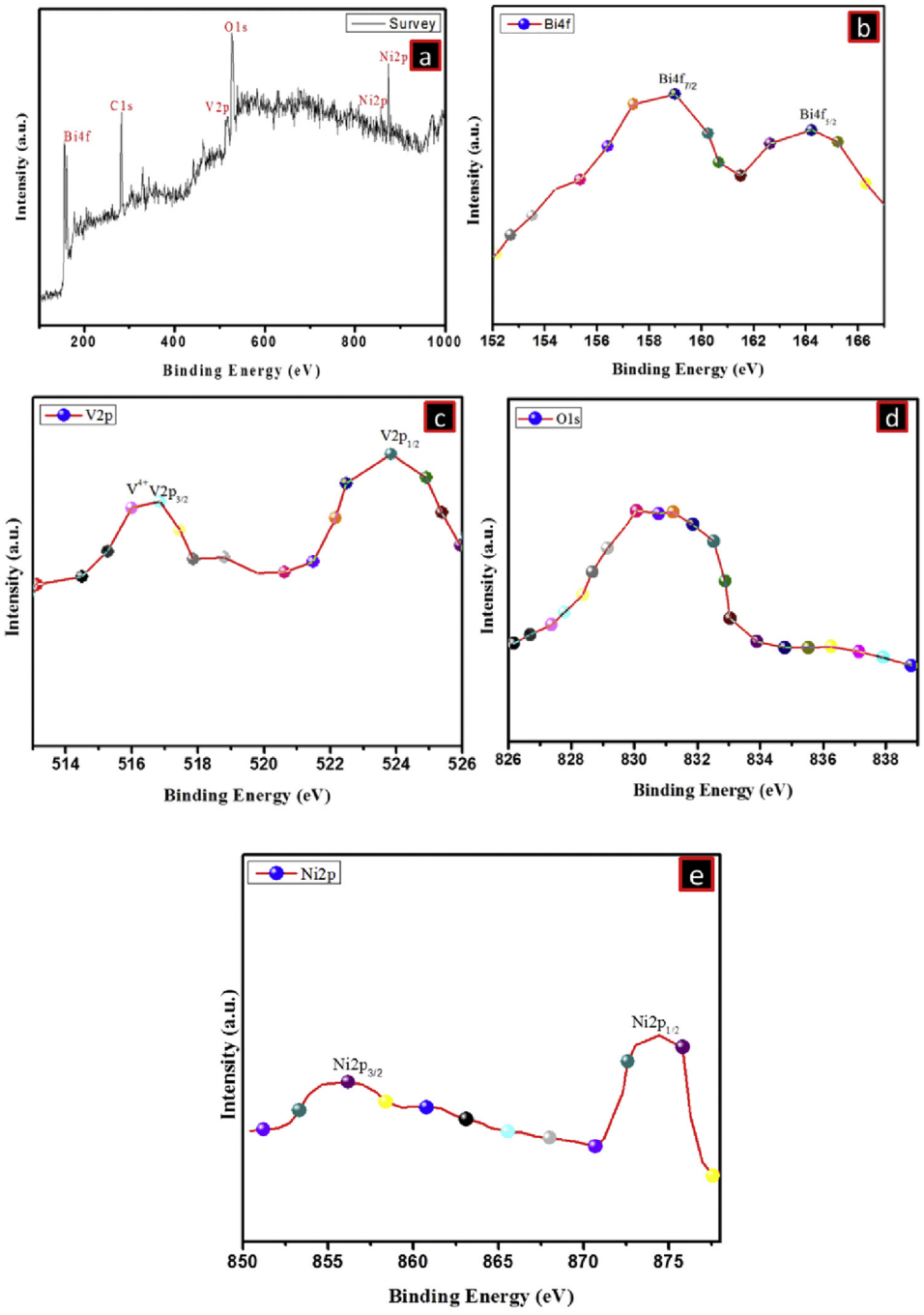

Fig. 5 – XPS spectra of Ni–$BiVO_4$ (N3) thin films; (a)Survey; (b)Bi4f; (c)V2p; (d)O1s; (e)Ni2p.

Photocurrent density analysis

Photocurrent density of the prepared thin films were calculated from current-voltage (I–V) graphs, recorded under dark and illumination, at a bias of −1 to 1 V/SCE (−0.34 to 1.65 V vs. RHE). 0.1 M KPi (pH 7) was used as electrolyte with and without the presence of hole scavenger (Na_2SO_3). Fig. 6(a and b) and Fig. S4 (Supplementary Information) represents the photocurrent density plots for P1, N3 and all other Ni doped samples respectively. Fig. 6 (a and b) clearly shows that there is enhancement in photocurrent density in case of Ni doping which is due to the increased carrier concentration and electrical conductivity which effectively results in better charge separation and enhanced PEC response [24,30]. In presence of hole scavenger enhancement in J_{ph} values was observed as compare to the absence of hole scavenger. This is because the hole scavenger acts as a electron donor and is very much capable to scavenge the photogenerated VB holes upon irradiation. The highest J_{ph} of 1.36 mA cm^{-2} at 1.23 V/RHE was obtained for 1.5% Ni doped $BiVO_4$ which was higher than that

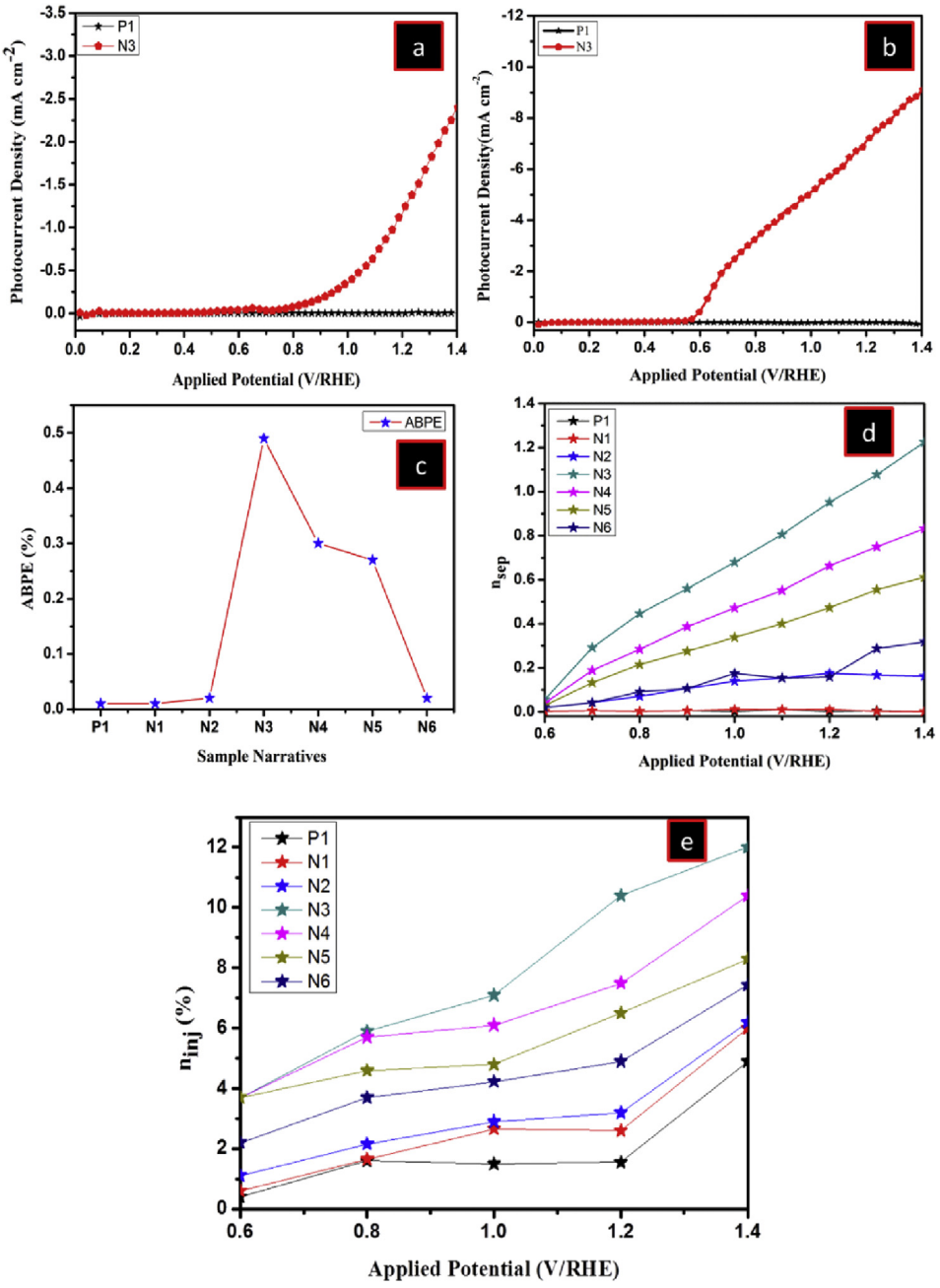

Fig. 6 – Linear sweep voltammetry for pristine $BiVO_4$ (P1) and Ni–$BiVO_4$ (N3) (a) 0.1 M KPi and (b) 0.1 M KPi + 0.1 M Na_2SO_3 (c) ABPE plot for pristine and Ni–$BiVO_4$ thin films (d) The calculated charge separation efficiency and (e) Charge injection efficiency of pristine and Ni–$BiVO_4$ thin films in 0.1 M KPi solution.

of pristine $BiVO_4$ (0.01 mA cm^{-2} at 1.23 V/RHE), due to the better separation of charge carriers [44].

Chopped light experiments were also performed under light on and off condition in the potential range of −1 V–1 V vs. SCE (−0.34 to 1.65 V vs. RHE) with and without the presence of hole scavenger and the results are shown in Fig. S4 (Supplementary Information). From the graphs it is observed that there is a positive correlation between current vs. applied potential. Various photoelectrochemical parameters obtained are given in Table 3.

The impact of Ni doping on the charge separation and charge injection efficiency at electrode/electrolyte interface was evaluated by providing the potential from 0.6 V to 1.4 V with respect to RHE using 0.1 M Na_2SO_4 as hole scavenger in 0.1 M KPi solution as shown in Fig. 6 (d,e). From the Fig. it is clear that P1 shows insignificant charge separation efficiency while N3 shows much higher charge separation in comparision to other samples. This enhancement in charge separation efficiency is due to the improved conductivity after doping. Further the information about charge transport was obtained with the help of charge injection efficiency. From the Figure it is clear that charge injection was higher for N3 sample in comparison to other samples. Based on this, we can conclude that separation and injection of photogenerated

Table 3 – PCD and ABPE of the electrodeposited thin films at 1.23 V/RHE.

Sample description	PCD (mA cm^{-2} at 1.23 V/RHE) in 0.1 M KPi without (Na_2SO_3)	PCD (mA cm^{-2} at 1.23 V/RHE) in 0.1 M KPi with (Na_2SO_3)	ABPE at 1.23 V/RHE
P1	0.01	0.03	0.01
N1	0.02	0.06	0.01
N2	0.06	1.18	0.02
N3	1.36	7.36	0.49
N4	0.82	5.10	0.30
N5	0.67	3.71	0.27
N6	0.06	1.87	0.02

charge carriers can be promoted with the enhanced conductivity [60]. Further the details related to both the efficiency are provided in Supplementary Information.

Open circuit potential (V_{OC}) which is defined as the potential at which there is no current. It is generally obtained by current-voltage (I–V) graph under illumination condition. The results obtained from the I–V graphs were used further to calculate ABPE of the prepared samples [44]. Table 2 shows the Voc of all the Ni doped $BiVO_4$ thin films in comparison to pristine one.

Mott-Schottky (M–S) analysis

The charge transfer kinetics and flat band potential of the thin films at semiconductor/electrolyte interface was determined through the Mott-Schottky analysis using 0.1 M KPi solution as electrolyte (Fig. 7). Mott-Schottky plots ($1/C^2$ vs. applied potential) for different samples in 0.1 M KPi are shown in Fig. S5 (Supplementary Information). n-type nature of the thin film was confirmed by the positive slope of the M–S plots. More negative flat band potential is assumed to be more favorable for water splitting reaction and is more important in terms of facilitating charge carrier transport [11]. Based on this analysis, it was found that V_{FB} is lower for N3 (0.37 eV) sample in comparison to all other samples.

Table 4 – Values of Resistance and Capacitance obtained from Randle's circuit fitting.

Sample identity	R1(Ω)	R2(Ω)	R3(Ω)	C2(F)	C3(F)
P1	55.65	305.9	3821	$3.3\ e^{-9}$	$1.1\ e^{-6}$
N3	29.73	103.6	1279	$6.67\ e^{-6}$	$3.3\ e^{-5}$

Further, Nyquist plot was studied to determine the charge transfer resistance at semiconductor/electrolyte interface. Charge transfer properties of the material depend upon the radii of semicircle, smaller the radii, superior will be the charge transfer property. To study the resistance at semiconductor/electrolyte interface, Randle's circuit was fit on the best sample and results are reported in Table 4 and Fig. 7 (c). In randle circuit there are 3 resistors (R1, R2 and R3) and two capacitors (C2 and C3). R2, C2 and R3, C3 are parallel to each other and corresponds to $BiVO_4$/Electrolyte and bulk $BiVO_4$ whereas, R1 corresponds to the solution resistance. Fig. 7 (c) shows Nyquist plot for P1 and N3 sample in electrolyte 0.1 M KPi solution. The M–S and Nyquist plot for all the samples in

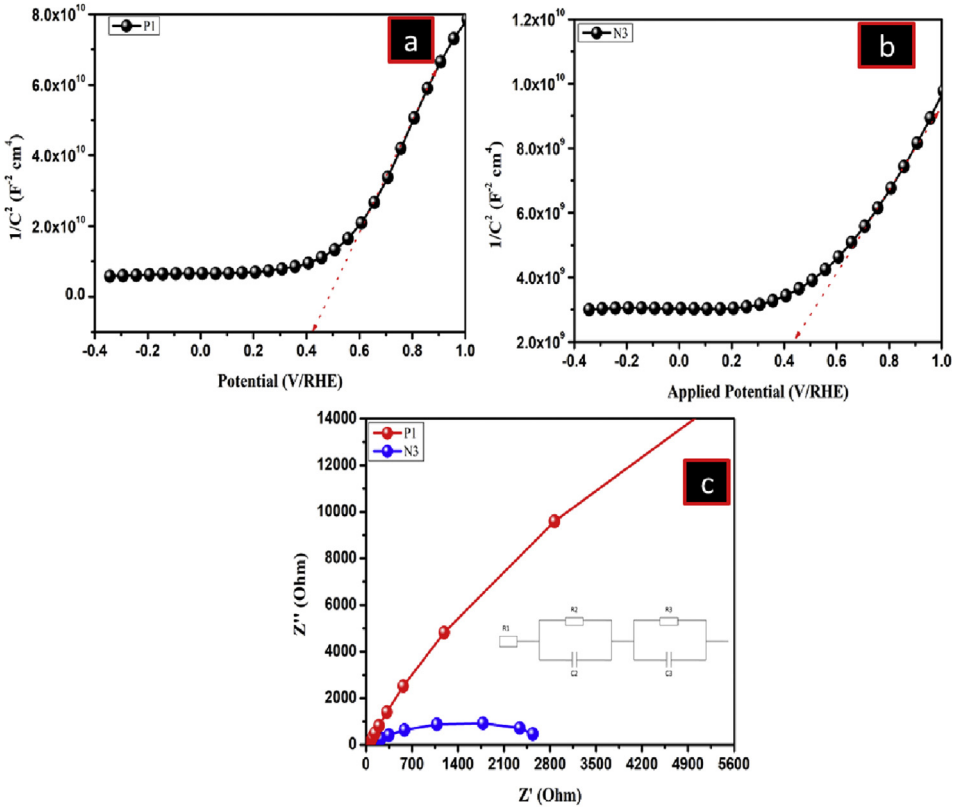

Fig. 7 – (a,b) Mott-Schottky plots and (c) Nyquist plot with equivalent circuit for pristine $BiVO_4$ (P1) and Ni–$BiVO_4$ (N3) in 0.1 M KPi solution (frequency: 1 kHz and amplitude: 5 mV).

0.1 M KPi solution are shown in Fig. S5 (Supplementary Information). In Fig. 7 (c) the radius of semicircle is least for the N3 sample, exhibiting least resistivity in 0.1 M KPi solution.

Efficiency measurement and chronoamperometric analysis

Efficiency of a semiconductor electrode depends upon the photocurrent density recorded through current-voltage curve. ABPE of all the samples were calculated using 150 W Xenon arc lamp and are shown in Fig. 6 (c). From the Fig. 6 (c) it is clear that maximum efficiency of 0.49% was obtained for N3 sample which is attributed to high open circuit potential, least charge transfer resistance and minimum flat band potential.

Finally, the stability of the best samples were tested by performing chronoamperometry using Zahner electrochemical work station for 3600s in KPi solutions under illumination at a potential of 1 V/SCE using three electrode systems and is shown in Fig. S4 (Supplementary Information). From the figure it is clear that N3 shows a stable current while in case of P1 the current is slightly decreases. This may be due to the presence of electron hole pair recombination.

The results reported in literature concerning similar studies are summarized in Table 5. PCD value of 1.5% Ni doped $BiVO_4$ is comparable with the previously reported results on doping in $BiVO_4$.

Table 5 – The PCD values reported so far with various dopants.

Sample description	Electrolyte	PCD values	Reference
Mo: $BiVO_4$	0.5 M phosphate buffer containing 0.5 M Na_2SO_3	2.93 mA/cm^2 at 1.23 V vs. RHE	[27]
Mo:$BiVO_4$	0.5 M Na_2SO_3 in 0.1 M potassium phosphate buffer solution	1.2 mA/cm^2 at 1.23 V vs. RHE	[32]
Mo−$BiVO_4$ and Co-Pi catalyzed Mo −$BiVO_4$	0.1 M KPi solution	1.9 mA/cm^2 and 4.6 mA/cm^2 at 1.23 V vs. RHE	[38]
Ni−$BiVO_4$	0.2 M Na_2SO_4	2.39 mA/cm^2 at 1.23VSCE	[40]
W doped Co-Pi catalyzed $BiVO_4$	0.5 M K_2SO_4 buffered with K_2HPO_4 and KH_2PO_4 an aq. 0.1 M KPi solution	2.3 mA/cm^2 at 1.23 V vs.RHE	[42]
Mo:$BiVO_4$	1 M NaOH	0.88 mA/cm^2 at 1.4 V vs. RHE	[48]
W:$BiVO_4$	0.5 M Na_2SO_4 solution	0.58 mA/cm^2 at 0.9 V vs. Ag/AgCl	[49]
n-n$^+$ Mn−$BiVO_4$	Na_2SO_4	2.2 mA/cm^2 at 1.0 V vs. SCE	[55]
W:$BiVO_4$	0.1 M K_2HPO_4 with and without Na_2SO_3	3.6 mA/cm^2 with and 2.25 mA/cm^2 without hole scavenger at 1.23VRHE	[60]
Mo:$BiVO_4$	0.1 M KPi + Na_2SO_3	4.15 mA/cm^2 at 1.23 V vs. RHE	[67]
Mo:$BiVO_4$	0.1 M Na_2SO_4	5.3 mA/cm^2 at 1.23 V vs. RHE	[68]
Ni−$BiVO_4$	0.1 M phosphate buffer containing 0.1 M Na_2SO_3	1.36 mA/cm^2 and 7.36 mA/cm^2 at 1.23 V/RHE without and with Na_2SO_3	This Study

Summary

Charge transfer mechanism in presence and absence of hole scavenger (Na_2SO_3)

Light illumination at the surface of semiconductor generates electron-hole pairs. By the oxidation -reduction reaction in the electrolyte (0.1 M KPi without hole scavenger) hydrogen and oxygen (Fig. 8a) produced at their respective electrodes. In presence of hole scavenger (Na_2SO_3) the photogenerated holes are scavenged by Na_2SO_3 and increase the yield of hydrogen production. The set of reactions taking place are written below: [63–66]:

Irradiation: $SO_3^{2-} \rightarrow SO_3^{2-*}$

Oxidation: $SO_3^{2-*} + 2OH^- \rightarrow SO_4^{2-} + H_2O + 2e^-$

Reduction: $2H_2O + 2e^- \rightarrow H_2 + 2OH^-$

Oxidation: $2SO_3^{2-} \rightarrow S_2O_6^{2-} + 2e^-$

Reduction: $2H_2O + 2e^- \rightarrow H_2 + 2OH^-$

The set of photoelectrochemical reactions taking place at photoanode using Na_2SO_3 as hole scavenger:

At working electrode:

$BiVO_4 + h\nu \rightarrow BiVO_4(h^+) + BiVO_4(e^-)$

$h^+ + SO_3^{2-} \rightarrow SO_4^{2-}$

At counter electrode:

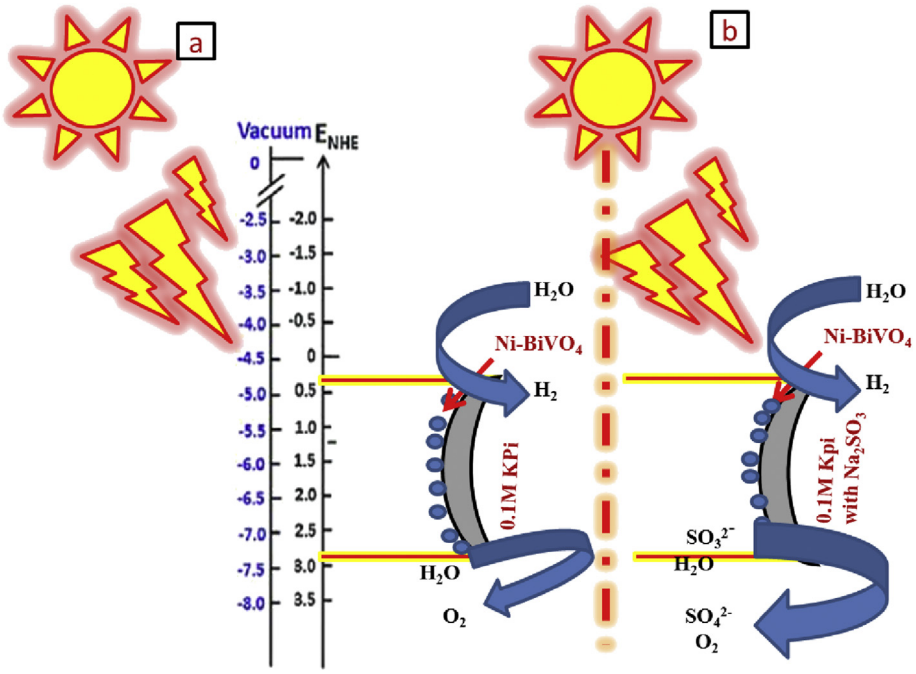

Fig. 8 – Charge transfer mechanism in absence and presence of hole scavenger.

$2H^+ + e^- \rightarrow H_2$

Conclusion

The present study is focused on the Ni–$BiVO_4$ photoanode fabrication for photoelectrochemical analysis in phosphate buffer electrolyte. Ni– $BiVO_4$ with varying Ni concentrations (0.5 atomic % to 3.0 atomic %) have been prepared in which 1.5% Ni doped $BiVO_4$ exhibited best response. 1.5% Ni doped $BiVO_4$ offers highest photocurrent density (1.36 mA cm^{-2} at 1.23 V vs. RHE), lower flat band potential, high open circuit potential and improved absorbance in the visible region. It was also observed that doped samples offer improved PEC response in comparison to pristine $BiVO_4$ due to the increase carrier concentration and electrical conductivity.

Declaration of competing interest

The authors declare that they have no known competing financial interests or personal relationships that could have appeared to influence the work reported in this paper.

Acknowledgements

This work is supported under the scheme of MNRE project (File No. 103/241/2015-NT). The author (Sakshi Saxena) also thankful to Department of Science & Technology, Ministry of Science & Technology, Govt. of India, for Inspire Fellowship (DST/INSPIRE Fellowship/2018/IF180375), (DST-FIST) and Inter University Accelerator Centre (IUAC), New Delhi for providing SEM, EDX and Raman Analysis facilities.

Appendix A. Supplementary data

Supplementary data to this article can be found online at https://doi.org/10.1016/j.ijhydene.2020.07.080.

REFERENCES

[1] Rodríguez-Castellanos A, López-Torres E, Solorza-Feria O. Solar-hydrogen-fuel cell prototype as a source of renewable energy generation. J. Mex. Chem. Soc 2007;51(2):55–8.
[2] Sharma D, Verma A, Satsangi VR, Shrivastav R, Dass S. Nanostructured $SrTiO_3$ thin films sensitized by Cu_2O for photoelectrochemical hydrogen generation. Int J Hydrogen Energy 2014;39(9):4189–97.
[3] Liu X, Iocozzia J, Wang Y, Cui X, Chen Y, Zhao S, Li Z, Lin Z. Noble metal-metal oxide nanohybrids with tailored nanostructures for efficient solar energy conversion. Photocatalysis and Environmental Remediation Energy Environ. Sci 2017;10(2):402–34.
[4] Chen Z, Jaramillo TF, Deutsch TG, Kleiman-Shwarsctein A, Forman AJ, Gaillard N, Garland R, Takanabe K, Heske C, Sunkara M, McFarland EW. Accelerating materials development for photoelectrochemical hydrogen production: standards for methods, definitions and reporting protocols. J Mater Res 2010;25(1):3–16.
[5] Li Y, Zhang JZ. Hydrogen generation from photoelectrochemical water splitting based on nanomaterials. Laser Photon Rev 2010;4(4):517–28.

[6] Turner J, Sverdrup G, Mann MK, Maness PC, Kroposki B, Ghirardi M, Evans RJ, Blake D. Renewable Hydrogen Production. Int. J. Energy Res. 2008;32(5):379–407.

[7] Brouwer J. On the role of fuel cells and hydrogen in a more sustainable and renewable energy future. Curr Appl Phys 2010;10(2):S9–17.

[8] Abinaya K, Karthikaikumar S, Sudha K, Sundharamurthi S, Elangovan A, Kalimuthu P. Synergistic effect of 9-(pyrrolidin-1-yl)perylene-3,4-dicarboximide functionalization of amino graphene on photocatalytic hydrogen generation. Sol Energy Mater Sol Cells 2018;185:431–8.

[9] Bak T, Nowotny J, Rekas M, Sorrell CC. Photo-electrochemical hydrogen generation from water using solar energy. Materials-related aspects. Int J Hydrogen Energy 2002;27(10):991–1022.

[10] Choudhary S, Upadhyay S, Kumar P, Singh N, Satsangi VR, Shrivastav R, Dass S. Nanostructured bilayered thin films in photoelectrochemical water splitting -A review. Int J Hydrogen Energy 2012;37(24):18713–30.

[11] Ikram A, Sahai S, Rai S, Dass S, Shrivastav R, Satsangi VR. Synergistic effect of CdSe quantum dots on photoelectrochemical response of electrodeposited α-Fe_2O_3 films. J Power Sources 2014;267:664–72.

[12] Kim JY, Magesh G, Youn DH, Jang JW, Kubota J, Domen K, Lee JS. Single-crystalline, wormlike hematite photoanodes for efficient solar water splitting. Sci Rep 2013;3:2681.

[13] Kumari B, Sharma S, Singh N, Verma A, Satsangi VR, Dass S, Shrivastav R. ZnO thin films, surface embedded with biologically derived Ag/Au nanoparticles, for efficient photoelectrochemical splitting of water. Int J Hydrogen Energy 2014;39(32):18216–29.

[14] Kumari S, Tripathi C, Singh AP, Chauhan D, Shrivastav R, Dass S, Satsangi VR. Characterization of Zn-doped hematite thin films for photoelectrochemical splitting of water. Curr Sci 2006;91(8):1062–4.

[15] Campet G, Deshayes A, Frison JC, Treuil N, Portier J. Applications of nanoscale materials in the fields of electrochemistry and photoelectrochemistry active and passive elec. COM 1998;21(2):123–46.

[16] Banerjee A, Mondal B, Verma A, Satsangi VR, Shrivastav R, Dey A, Dass S. Enhancing eefficiency of Fe_2O_3 for robust and proficient solar water splitting using a highly dispersed bioinspired catalyst. J Catal 2017;352:83–92.

[17] Verma A, Srivastav A, Sharma D, Banerjee A, Sharma S, Satsangi VR, Shrivastav R, Avasthi DK, Dass S. A study on the effect of low energy ion Beam irradiation on Au/TiO_2 system for its application in photoelectrochemical splitting of water nuc. Instrum. Methods Phys. Res. B 2016;379:255–61.

[18] Tolod KR, Hernández S, Russo N. Recent advances in the $BiVO_4$ photocatalyst for sun-driven water oxidation. Top-Performing Photoanodes and Scale-Up Challenges Catalysts 2017;7(1):13.

[19] Hernández S, Gerardi G, Bejtka K, Fina A, Russo N. Evaluation of the charge transfer kinetics of spin-coated $BiVO_4$ thin films for sun-driven water photoelectrolysis. Appl Catal B 2016;190:66–74.

[20] Prakash A, Dan M, Yu S, Wei S, Li Y, Wang F, Zhou Y. In_2S_3/CuS nanosheet composite: an excellent visible light photocatalyst for H_2 production from H_2S. Sol Energy Mater Sol Cells 2018;180:205–12.

[21] Srivastav A, Verma A, Banerjee A, Khan SA, Gupta M, Satsangi VR, Shrivastav R, Dass S. Gradient doping – a case study with Ti-Fe_2O_3 towards an improved photoelectrochemical response. Phys Chem Chem Phys 2016;18(48):32735–43.

[22] Bard AJ, Fox MA. Artificial photosynthesis: solar splitting of water to hydrogen and oxygen. Acc Chem Res 1995;28(3):141–5.

[23] Tseng CJ, Tseng CL. The reactor design for photoelectrochemical hydrogen production. Int J Hydrogen Energy 2011;36(11):6510–8.

[24] Kim JH, Lee JS. $BiVO_4$-Based heterostructured photocatalysts for solar water splitting: a review energy environ. Focus 2014;3(4):339–53.

[25] Solanki A, Shrivastava J, Upadhyay S, Sharma V, Sharma P, Kumar P, Kumar P, Gaskell K, Satsangi VR, Shrivastav R, Dass S. Irradiation-induced modifications and PEC response - a case study of $SrTiO_3$ thin films irradiated by 120 MeV Ag^{9+} ion. Int J Hydrogen Energy 2011;36(9):5236–45.

[26] Cheng BY, Yang JS, Cho HW, Wu JJ. Fabrication of efficient $BiVO_4$-TiO_2 heterojunction photoanode for photoelectrochemical water oxidation. ACS Appl Mater Interfaces 2016;8(31):20032–9.

[27] Qiu Y, Liu W, Chen W, Zhou G, Hsu PC, Zhang R, Liang Z, Fan S, Zhang Y, Cui Y. Efficient solar-driven water splitting by nanocone $BiVO_4$-perovskite tandem cells sci. Adv 2016;2(6):e1501764.

[28] Hilliard S, Friedrich D, Kressman S, Strub H, Artero V, Laberty-Robert C. Solar water splitting $BiVO_4$ thin film photoanodes by sol-gel dip coating technique. ChemPhotoChem 2017;1(6):273–80.

[29] Dunkle SS, Helmich RJ, Suslick KS. $BiVO_4$ as a visible-light photocatalyst prepared by ultrasonic spray pyrolysis. J Phys Chem C 2009;113(28):11980–3.

[30] Yaw CS, Chong MN, Soh AK. Bismuth vanadate-based photoelectrodes for photoelectrochemical water splitting: synthesis and characterisation. Trans Tech Publications 2017;99:9–16.

[31] Lu Y, Luo YS, Xiao HM, Fu SY. Novel core–shell structured $BiVO_4$ hollow spheres with an ultra-high surface area as visible-light-driven catalyst. CrystEngComm 2014;16(27):6059–65.

[32] Gong H, Freudenberg N, Nie M, Van de, Krol R, Ellmer K. $BiVO_4$ photoanodes for water splitting with high injection efficiency, deposited by reactive magnetron Co-sputtering. AIP Adv 2016;6(4):045108. 11.

[33] Park Y, McDonald KJ, Choi KS. Progress in bismuth vanadate photoanodes for use in solar water oxidation. Chem Soc Rev 2013;42(6):2321–37.

[34] Jia Q, Iwashina K, Kudo A. Facile fabrication of an efficient $BiVO_4$ thin film electrode for water splitting under visible light irradiation. Proc Natl Acad Sci Unit States Am 2012;109(29):11564–9.

[35] Tan HL, Amal R, Ng YH. Alternative strategies in improving the photocatalytic and photoelectrochemical activities of visible light-driven $BiVO_4$: a review. J Mater Chem A 2017;5(32):16498–521.

[36] Onishi T, Fujishima M, Tada H. Solar-driven one-compartment hydrogen peroxide-photofuel cell using bismuth vanadate photoanode. ACS Omega 2018;3(9):12099–105.

[37] Quinonero J, Lana–Villarreal T, Gómez R. Improving the photoactivity of bismuth vanadate thin film photoanodes through doping and surface modification strategies. Appl Catal B 2016;194:141–9.

[38] Rohloff M, Anke B, Zhang S, Gernert U, Scheu C, Lerch M, Fischer A. Mo-doped $BiVO_4$ thin films – high photoelectrochemical water splitting performance achieved by a tailored structure and morphology sustain. Energy & Fuels 2017;1(8):1830–46.

[39] Regmi C, Kshetri YK, Kim TH, Pandey RP, Ray SK, Lee SW. Fabrication of Ni-doped $BiVO_4$ semiconductors with enhanced visible-light photocatalytic performances for wastewater treatment appl. Surf Sci 2017;413:253–65.

[40] Kong D, Qi J, Liu D, Zhang X, Pan L, Zou J. Ni-doped $BiVO_4$ with V^{4+} species and oxygen vacancies for efficient

photoelectrochemical water splitting Trans. Tianjin Univ 2019;25(4):340–7.
[41] Merupo V, Velumani S, Kassiba A, García-Sánchez MA. Structural and optical properties of molybdenum doped bismuth vanadate powders. In: 11th International Conference on Electrical Engineering, Computing Science and Automatic Control (CCE); 2014. p. 1–5.
[42] Abdi FF, Firet N, Van de, Krol R. Efficient $BiVO_4$ thin film photoanodes modified with cobalt phosphate catalyst and W-doping. ChemCatChem 2013;5(2):490–6.
[43] Su J, Guo L, Bao N, Grimes CA. Nanostructured $WO_3/BiVO_4$ heterojunction films for efficient photoelectrochemical water splitting. Nano Lett 2011;11(5):1928–33.
[44] Verma A, Srivastav A, Khan SA, Satsangi VR, Shrivastav R, Avasthi DK, Dass S. Enhanced photoelectrochemical response of plasmonic Au embedded $BiVO_4/Fe_2O_3$ heterojunction. Phys Chem Chem Phys 2017;19(23):15039–49.
[45] Kalanur SS, Yoo IH, Park J, Seo H. Insights into electronic bands of $WO_3/BiVO_4/TiO_2$, revealing high solar water splitting efficiency. J Mater Chem A 2017;5(4):1455–61.
[46] Hong SJ, Lee S, Jang JS, Lee JS. Heterojunction $BiVO_4/WO_3$ electrodes for enhanced photoactivity of water oxidation energy. Environ Sci 2011;4(5):1781–7.
[47] Zhang K, Shi XJ, Kim JK, Park JH. Photoelectrochemical cells with tungsten trioxide/Mo-doped $BiVO_4$ bilayers. Phys Chem Chem Phys 2012;14(31):11119–24.
[48] Li L, Yang X, Lei Y, Yu H, Yang Z, Zheng Z, Wang D. Ultrathin Fe-NiO nanosheets as catalytic charge reservoirs for a planar Mo- doped $BiVO_4$ photoanode. Chem Sci 2018;9(47):8860–70.
[49] Wan X, Niu F, Su J, Guo L. Enhanced photoelectrochemical water oxidation of bismuth vanadate via a combined strategy of W doping and surface RGO modification. Phys Chem Chem Phys 2016;18(46):31803–10.
[50] Zhao D, Wang W, Sun Y, Fan Z, Du M, Zhang Q, Ji F, Xu X. One-step synthesis of composite material MWCNT@$BiVO_4$ and its photocatalytic activity. RSC Adv 2017;7(53):33671–9.
[51] Toma FM, Cooper JK, Kunzelmann V, McDowell MT, Yu J, Larson DM, Borys NJ, Abelyan C, Beeman JW, Yu KM, Yang J. Mechanistic insights into chemical and photochemical transformations of bismuth vanadate photoanodes. Nat Commun 2016;7:1–11.
[52] Seabold JA, Choi KS. Efficient and stable photo-oxidation of water by a bismuth vanadate photoanode coupled with an iron oxyhydroxide oxygen evolution catalyst. J Am Chem Soc 2012;134(4):2186–92.
[53] Kim TW, Choi KS. Nanoporous $BiVO_4$ photoanodes with dual-layer oxygen evolution catalysts for solar water splitting. Sci 2014;343(6174):990–4.
[54] Zhang K, Jin B, Park C, Cho Y, Song X, Shi X, Zhang S, Kim W, Zeng H, Park JH. Black phosphorene as a hole extraction layer boosting solar water splitting of oxygen evolution catalysts nat. Commun Now 2019;10(1):2001.
[55] Srivastav A, Kumar P, Verma A, Smith YR, Satsangi VR, Shrivastav R, Waghmare UV, Dass S. Experimental and first-principles studies of $BiVO_4/BiV_{1-x}MnxO_4$-y n-n^+ homojunction for efficient charge carrier separation in sunlight induced water splitting. Int J Hydrogen Energy 2018;43(33):15815–22.
[56] Tiwari JN, Tiwari RN, Kim KS. Zero-dimensional, one-dimensional, two-dimensional and three-dimensional nanostructured materials for advanced electrochemical energy devices. Prog Mater Sci 2012;57(4):724–803.
[57] Liu EY, Thorne JE, He Y, Wang D. Understanding photocharging effects on bismuth vanadate. ACS Appl Mater Interfaces 2017;9(27):22083–7.
[58] Hilliard S, Friedrich D, Kressman S, Strub H, Artero V, Laberty-Robert C. Solar water splitting $BiVO_4$ thin film photoanodes by sol-gel dip coating technique. ChemPhotoChem 2017;1(6):273–80.
[59] Ma Y, Mesa CA, Pastor E, Kafizas A, Francàs L, Le Formal-F, Pendlebury SR, Durrant JR. Rate law analysis of water oxidation and hole scavenging on a $BiVO_4$ photoanode. ACS Energy Lett 2016;1(3):618–23.
[60] Prasad U, Prakash J, Azeredo B, Kannan A. Stoichiometric and non-stoichiometric tungsten doping effect in bismuth vanadate based photoactive material for photoelectrochemical water splitting electrochim. Acta 2019;299:262–72.
[61] Luo W, Wang J, Zhao X, Zhao Z, Li Z, Zou Z. formation energy and photoelectrochemical properties of $BiVO_4$ after doping at Bi^{3+} or V^{5+} sites with higher valence metal ions. Phys Chem Chem Phys 2013;15(3):1006–13.
[62] Cho SK, Park HS, Lee HC, Nam KM, Bard AJ. Metal doping of $BiVO_4$ by composite electrodeposition with improved photoelectrochemical water oxidation. J Phys Chem C 2013;117(44):23048–56.
[63] Schneider J, Bahnemann DW. Undesired role of sacrificial reagents in photocatalysis. J Phys Chem Lett 2013;4:3479–83.
[64] Kumaravel V, Imam MD, Badreldin A, Chava RK, Do JY, Kang M, Abdel-Wahab A. Photocatalytic hydrogen production: role of sacrificial reagents on the activity of oxide. Carbon,and Sulfide Catalysts Catalysts 2019;9(3):276.
[65] Ni M, Leung MK, Leung DY, Sumathy K. A review and recent developments in photocatalytic water-splitting using TiO_2 for hydrogen production. Renew. Sust. Energ Rev 2007;11(3):401–25.
[66] Mahadik MA, Chung HS, Lee SY, Cho M, Jang JS. In-situ noble fabrication of $Bi_2S_3/BiVO_4$ hybrid nanostructure through a photoelectrochemical transformation process for solar hydrogen production. ACS Sustain Chem Eng 2018;6(9):12489–501.
[67] Wang Z, Dong C, Liang S, Yao S, Wang Z, Zeng Q, Liu C, Liu Y, Yang B, Zhang H. Preparation of textured and transparent $BiVO_4$ photoelectrodes based on Mo-doped $BiVO_4$ nanoparticles for constructing a stand-alone tandem water splitting device. ChemComm 2020;56(30):4156–9.
[68] Subramanyam P, Vinodkumar T, Nepak D, Deepa M, Subrahmanyam C. Mo-doped $BiVO_4$@reduced graphene oxide composite as an efficient photoanode for photoelectrochemical water splitting Catal. Today Off 2019;325:73–80.
[69] Rafiei-Sarmazdeh Zahra, Zahedi-Dizaji Seyed Morteza, Kang Aniseh Kafi. Two-Dimensional Nanomaterials In Nanostructures. IntechOpen; 2019.